

Steady and unsteady shear flows of a viscoplastic fluid in a cylindrical Couette cell

Laurent Lacaze, Audrey Filella, Olivier Thual

▶ **To cite this version:**

Laurent Lacaze, Audrey Filella, Olivier Thual. Steady and unsteady shear flows of a viscoplastic fluid in a cylindrical Couette cell. Journal of Non-Newtonian Fluid Mechanics, 2015, vol. 220, pp. 126 -136. 10.1016/j.jnnfm.2014.12.009 . hal-01226458

HAL Id: hal-01226458
https://hal.science/hal-01226458

Submitted on 9 Nov 2015

HAL is a multi-disciplinary open access archive for the deposit and dissemination of scientific research documents, whether they are published or not. The documents may come from teaching and research institutions in France or abroad, or from public or private research centers.

L'archive ouverte pluridisciplinaire **HAL**, est destinée au dépôt et à la diffusion de documents scientifiques de niveau recherche, publiés ou non, émanant des établissements d'enseignement et de recherche français ou étrangers, des laboratoires publics ou privés.



Open Archive TOULOUSE Archive Ouverte (OATAO)
OATAO is an open access repository that collects the work of Toulouse researchers and makes it freely available over the web where possible.

This is an author-deposited version published in : http://oatao.univ-toulouse.fr/
Eprints ID : 14438

To link to this article : doi: 10.1016/j.jnnfm.2014.12.009
URL : http://dx.doi.org/10.1016/j.jnnfm.2014.12.009

To cite this version : Lacaze, Laurent and Filella, Audrey and Thual, Olivier Steady and unsteady shear flows of a viscoplastic fluid in a cylindrical Couette cell. (2015) Journal of Non-Newtonian Fluid Mechanics, vol. 220. pp. 126 -136. ISSN 0377-0257

Any correspondance concerning this service should be sent to the repository administrator: staff-oatao@listes-diff.inp-toulouse.fr

Steady and unsteady shear flows of a viscoplastic fluid in a cylindrical Couette cell

L. Lacaze [a,b,*], A. Filella [a], O. Thual [a]

[a] Université de Toulouse, INPT, UPS, IMFT (Institut de Mécanique des Fluides de Toulouse), Allée Camille Soula, F-31400 Toulouse, France
[b] CNRS, IMFT, F-31400 Toulouse, France

Keywords:
Visco-plastic fluid
Elasticity
Shear flows

A B S T R A C T

Yield stress fluid flows in Couette cells have been widely studied in the last decades for their intriguingly exhibiting phenomena. In this paper, we use a PIV technique to investigate the axisymmetric flow and rheological properties of a Carbopol gel in a relatively wide cylindrical Couette device. Carbopol gel is known to exhibit viscoplastic behavior and is often described using a Herschel–Bulkley law, which is characterized by a plastic yield stress τ_y and a shear-dependent nonlinear viscosity. In some cases, the elasticity of the material has to be accounted for to understand the whole dynamics of the system, in particular for unsteady flows as observed in the present study. Two set of experiments are conducted here in order to highlight these different rheological behaviors and the resulting dynamics: (i) a steady shear configuration and (ii) an unsteady shear configuration, in which the angular velocity of the inner cylinder is either constant or time dependent (sin profile), respectively. In the steady configuration, a simple optimization model, based on the Herschel–Bulkley law, is developed to extract the rheological parameters of the viscoplastic contribution of the gel from the steady velocity fields. Results are shown to be in good agreements with rheological parameters obtained from a standard rheometer. On the other hand, the elastic contribution of the material is highlighted in the unsteady shear configuration, for which a spatio-temporal transition between solid-elastic and fluid behaviors is observed. Different models are proposed to describe the dynamics of the unsteady flow. First, quasi-steady state models allow to predict both the fluid shear zone close to the inner cylinder and the elastic deformation of the material as long as their contributions can be decoupled in space and in time. For more complex dynamics, i.e. when the flow becomes strongly unsteady, an elasto-viscoplastic model is developed to describe the flow dynamics. It is shown to quantitatively reproduce the experimental measurements. Finally, an elastic wave model is derived to describe an elastic front propagating from the inner cylinder to the outer one, and observed at every half forcing period. The front velocity is thus shown to scale on the phase velocity of an elastic wave in a deformable solid.

1. Introduction

Viscoplastic fluids are encountered in many applications ranging from industries to geophysical flows, and have therefore attracted many studies dedicated to the improvement of their modeling. The presence of a yield stress in these fluids can drastically modify their flow dynamics compared with newtonian fluids. The simplest and most popular model, the Bingham model, consists in a solid-like behavior below a yield stress while the stress to strain relationship is linear above it. Yet, yield stress fluids found in nature or used in laboratory experiments, such as carbopol or laponite among others, highlight a non-linear trend above the plastic threshold, the shear stress τ being usually modeled through a power law of the shear rate $\dot{\gamma}$. A popular extension of the Bingham model, which accounts for these specific characteristics is the Herschel–Bulkley model, reading $\tau(\dot{\gamma}) = \tau_y + K\dot{\gamma}^n$, in which the three parameters τ_y, K and n depend on the considered material. In this model, $n < 1$ therefore correspond to a shear-thinning behavior above plasticity, i.e. a decrease of the apparent viscosity with increasing shear rate, which is commonly considered in the literature. A vast literature is devoted to the characterization of complex fluids to identify reliability and failure of this model to describe the dynamics of viscoplastic fluids (see the recent review [1] and references therein for instance).

* Corresponding author at: IMFT (Institut de Mécanique des Fluides de Toulouse), Allée Camille Soula, F-31400 Toulouse, France. Tel.: +33 53432 2952; fax: +33 53432 2990.
E-mail address: laurent.lacaze@imft.fr (L. Lacaze).

Viscoplastic fluids can also exhibit elasticity, at least prior yielding [2], which has been shown to influence the flow dynamics in some specific configurations [3–5]. Models accounted for elasticity can be found in the literature (see [6,7] for instance) and have been successfully tested [4,8,5,9]. Even if elasticity would be expected to influence mostly transient, it has been shown that it can also affect the steady state of the axisymmetric Couette flow [5]. It was explained by the normal stress difference within the cell gap. In particular, the initial stress condition was shown to modify the shape of the matching zone between solid and the fluid regions. In order to characterize the complex dynamics of such elasto-viscoplastic fluids, experimental investigations of simple flow configurations are still required.

The cylindrical Couette configuration remains probably one of the most popular experimental configuration used to characterize the dynamics of non-newtonian fluids, probably for the apparent simplicity of the system ([13–16,12,5,9] among others). In particular, this configuration allows to describe localized shear flows in viscoplastic gels, which have been deeply investigated for the last decades. In the present study, the case of this canonical cylindrical Couette configuration is revisited, using a relatively wide facility compared with the cells found in the literature. Note that among other complex behaviors, shear banding (see [10,11] and references therein) have been observed in laboratory experiments using relatively small gap cells. The experimental facility used here is large compared with the meso-structure of the gel, in which case these effects can be disregarded [12]. It consists of a two co-axial cylinders system, the inner cylinder being free to rotate and the outer one being fixed. The fluid used in the experimental part of the study is a Carbopol 940 gel, which is one of the most popular viscoplastic fluid used in laboratory experiments because of its rheological and transparency properties. Its rheological properties are therefore well documented (see [17,18,2,19] and references therein for instance). In the present study, the flow in the cell gap is generated by either a constant or an oscillatory angular velocity of the inner cylinder, referred to as the *steady shear configuration* and the *unsteady shear configuration* respectively. Unlike most of the experiments on this device, we develop here a PIV method, allowing to extract the velocity fields within the cell gap. The obtained velocity fields are then analyzed to characterize both (i) the flow dynamics and (ii) the rheological properties of the Carbopol gel.

The paper is organized as follows. We first introduce the rheological properties of the fluid considered here and present both the experimental set-up and the PIV method in Section 2. In Section 3, results associated with the steady shear configuration are discussed with a specific attention paid to an inverse method allowing to extract the rheological parameters of the gels. In Section 4, the unsteady shear configuration is presented in details and discussed in the light of several models. Finally, conclusions are drawn in Section 5.

2. Experimental procedure

2.1. Carbopol gel

The fluid used in the following experiments is a Carbopol 940 gel. Two different concentrations of Carbopol are considered here, which are 0.11% and 0.2% in weight and will be referred to as Carbopol *A* and Carbopol *B* respectively. Silver-coated hollow glass spheres of 10 μm diameter are used as seed particles for PIV measurements.

Bulk rheological measurements of the Carbopol solutions were performed using a Thermo-Scientific HAAKE Mars III rheometer with a plate-plate geometry. Rough plate surfaces were used to avoid wall slip [20,17]. Steady-state and oscillatory shear measurements were performed to obtain both the shear stress τ as a function of the strain rate $\dot{\gamma}$ (see Fig. 1(a)) and the elastic shear modulus G as a function of the strain γ, expressed here in % (see Fig. 1(b)), respectively.

As noticed in previous studies, the constant shear measurements show that above the yield stress, in the viscous region, the shear stress can be considered as a unique function of strain rate in the condition of atmospheric pressure and constant temperature (20 °C) considered here. It is common to consider that the steady flow behavior of Carbopol gel exhibits a τ to $\dot{\gamma}$ relationship that can be modeled by the Herschel–Bulkley model $\tau = \tau_y + K\dot{\gamma}^n$ with τ_y the yield stress, K the consistency and n the index. In Fig. 1(a), measurements (dot symbols) obtained using the rheometer and their best fit by the Herschel–Bulkley model (dotted lines) are shown for both Carbopol *A* (black) and Carbopopl *B* (gray). It can be observed that the Herschel–Bulkley model is relevant in the range of strain rates considered here. The coefficients τ_y, K and n obtained with this model are reported in Table 1 for both carbopol gels. Note that these values are consistent with data found in the literature for this gel ([2] for instance). In the oscillatory measurements, a sinusoidal shear strain is applied with a frequency of oscillation set to 1 Hz. Measurements found in the literature showed that results are not significantly affected by this frequency in the range 0.1–10 Hz [2,4]. In Fig. 1(b), the in-phase response G to the unsteady shear strain is shown to be nearly constant for small deformations γ of the sample, indicating an elastic response of the sample. Dotted lines represent the estimated value of G, in this elastic regime, for both Carbopol *A* and Carbopol *B*, which is also reported in Table 1. For larger γ, a sudden decrease of G highlights the solid to fluid transition of the visco-plastic material (see [19] for instance). Note that the critical deformation, which can be estimated as $\gamma_c \equiv \tau_y/G$ would be around 11% and 17% for Carbopol *A* and Carbopol *B* respectively, using the yield stress τ_y and constant G in the elastic regime extracted from these rheometric measurements. Even if the experimental evaluation of the critical deformation γ_c would necessitate dedicated rheometric measurements, which are beyond the scope of this paper, one can note that these estimations of γ_c correspond to the change of trend of G for increasing γ in Fig. 1(b). Finally, the viscous loss modulus G'', the out-of phase component of the stress response, shows to be at least one order of magnitude smaller than the elastic modulus G indicating that the gel is mostly elastic, at least below the yield stress (see Table 1).

2.2. Experimental set-up

The experimental set up is sketched in Fig. 2. The cylindrical Couette cell of height $H = 25$ cm is composed of an inner cylinder of radius $R_i = 7$ cm and a fixed outer cylinder of radius $R_o = 14$ cm. The outer cylinder is glued to the bottom of a square tank, both made of transparent plexiglass, allowing to illuminate the internal zone of measurement with an external light source (see Fig. 2). The Couette cell is filled with the Carbopol solution up to a height of around 20 cm while the surrounding tank is filled with water to prevent unexpected temperature fluctuations. The room temperature is set to 20 °C with an accuracy of less than 0.5 °C. The inner cylinder is covered of a ∼250 μm sand layer glued on its surface to ensure a no-slip boundary condition. A motor is connected to the inner cylinder, which allows to apply a constant or time-dependent angular velocity Ω_i. The maximum amplitude of the angular velocity is around 50 rpm. In the following, two cases are considered. First, a constant angular velocity $\Omega_i = \Omega_0$, leading to a steady regime, is referred here to as the *steady shear configuration*. In this case, the transient evolution towards this steady regime is disregarded. The second case is an oscillatory forcing such as

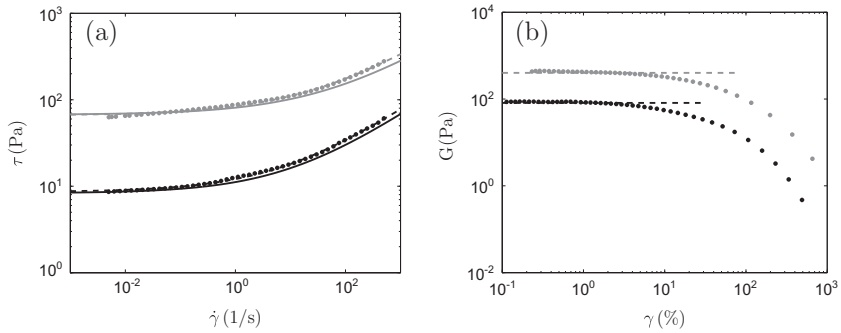


Fig. 1. Rheometric measurements using the Thermo-Scientific HAAKE Mars III rheometer for Carbopol *A* (black symbols) and Carbopol *B* (gray symbols). (a) τ as a function of $\dot{\gamma}$ ('dashed lines': best fit using a Herschel–Bulkley model, and 'solid line': results obtained from the inverse method described in Section 3.2). (b) Elastic modulus G a function of the deformation γ ('dashed lines': constant estimation for $\tau < \tau_y$).

Table 1
Top row: rheological parameters obtained using the Thermo-Scientific HAAKE Mars III rheometer. Bottom row: Rheological parameters evaluated from inverse method in the steady shear configuration (see Section 3.2 for details).

	Weight (%)	τ_y (Pa)	K (Pa s^n)	n	G (Pa)	G'' (Pa)
Carbopol *A*	0.11	8.6	3.5	0.43	81.5	5.8
Carbopol *B*	0.2	66	18	0.39	401.5	25
Carbopol *A*	0.11	8.3	2.9	0.44		
Carbopol *B*	0.2	67.1	14	0.4		

$\Omega_i = \Omega_0 \sin(\omega t)$ with Ω_0 and ω the amplitude and the frequency of the forcing respectively. This case will be referred to as the *unsteady shear configuration*. The latter configuration is somewhat the axisymmetric version of the second Stokes problem of an oscillatory plate in a semi infinite domain. Such plate geometry has been considered for the case of a viscoplastic fluid by [21].

As the gel is transparent, a PIV method can be implemented to measure the 2D velocity field in a horizontal plane. The chosen horizontal plane is here 10 cm above the bottom of the tank, roughly at the mid height of the cell. PIV measurements are performed with a Quantel CFR 200 mJ laser and 2040 × 2040 pixels 14-bit CCD camera. In order to avoid issues with optical access in the annular geometry, a telecentric lens is connected to the camera. The obtained field of interest is 15 × 15 cm^2. A spatial correlation technique, developed by [22], is used to extract velocity fields from pairs of consecutive images. The time interval between the two consecutive images is adjusted for each experiment, in particular depending on the maximum angular velocity Ω_0. Its range of variation is between 3 ms and 30 ms while the acquisition frequency, between each image pair, is set to 5 Hz for all experiments.

A typical image recorded by the camera is shown in Fig. 3(a). As shown in this figure, the field of measurement is roughly a quarter of the entire Couette cell. Image contrast is shown to be high enough to ensure an accurate cross-correlation calculation needed for the velocity field reconstruction. A typical velocity field is shown in Fig. 3(b). As the obtained ratio of radial to azimuthal velocities is of the order of 1%, only the azimuthal component of the velocity is considered in the following. Moreover, the flow is mostly axisymmetric, the forcing being low enough to prevent any instability of the flow. An azimuthal average of the velocity field can therefore be performed prior analyzing experimental data. The obtained average azimuthal velocity is denoted v in the

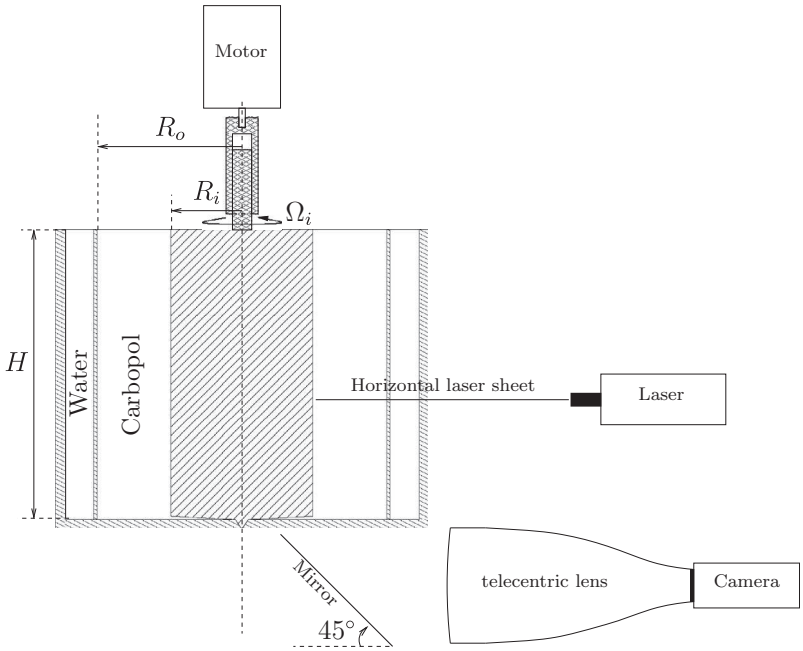


Fig. 2. Sketch of the experimental set-up.

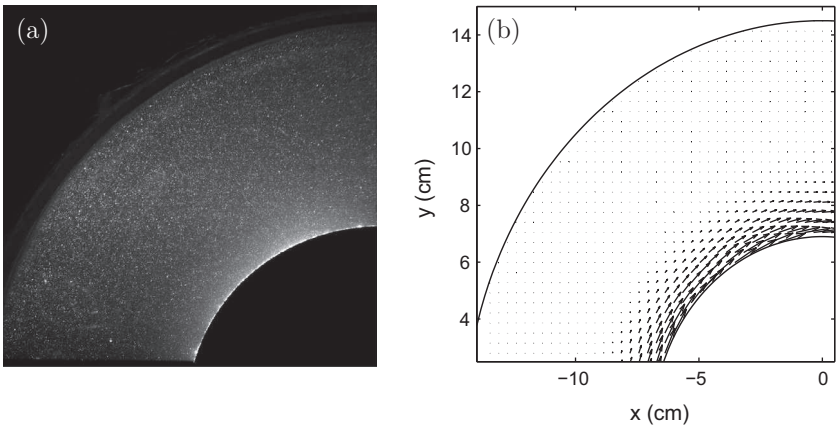


Fig. 3. Typical results from PIV. (a) Raw image recorded by the camera. (b) Velocity field: note that, for sake of clarity, the spatial resolution shown in this figure is half the spatial resolution of the grid used for velocity field reconstruction.

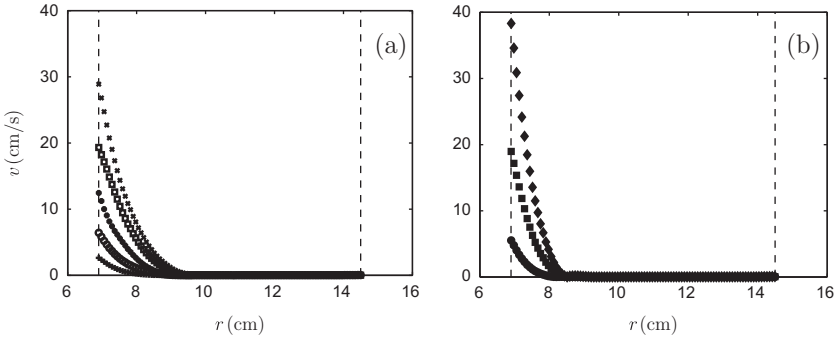


Fig. 4. Radial profiles of the azimuthal velocity v for Carbopol A (a) and Carbopol B (b) in the steady shear regime. Different symbols stand for different values of Ω_0.

following, and is only a function of the radial coordinate r and time t.

3. The steady shear configuration

3.1. Velocity profiles

Steady radial velocity profiles v obtained for a constant angular velocity $\Omega_i = \Omega_0$ applied to the inner cylinder are shown for both solutions A and B in Fig. 4(a) and (b) respectively. As can be expected for viscoplastic fluids, velocity profiles show to rapidly decrease towards zero for increasing r [14], highlighting a fluid to solid transition. The radial extension of the shear band (fluid region) is shown to depend upon the amplitude Ω_0 and the yield stress τ_y. This gives access to a first estimation of the position of the yield surface, which occurs in the present set of experiment between $r \sim 8$ cm and $r \sim 9.5$ cm.Even though a specific characterization of the flow dynamics close to the yield position would be of interest [5], it is beyond the scope of the present study and will not be investigated in more details here. Instead, the characteristics of the steady velocity profiles are used in the following to access the steady rheological properties of the gel.

3.2. An inverse method to estimate the steady state visco-plastic rheology

We propose here a method to extract the rheological parameters of the gel, considering a Herschel–Bulkley law, from the velocity field. This method consists in an optimization algorithm as described in the following. First, it can be noticed that in the present geometry and for a steady state flow, the shear to torque relationship reads [23]

$$\tau(r) = \frac{M}{2\pi r^2 H} = \frac{\mathcal{A}}{r^2}, \tag{1}$$

$$\tau(r) = \frac{M}{2\pi r^2 H} = \frac{\mathcal{A}}{r^2}, \tag{1}$$

with H the height of Carbopol gel in the Couette cell, M the applied torque, and $\mathcal{A} = M/2\pi H$ is independent of the radial coordinate.

Using the Herschel–Bulkley model, Eq. (1) can be written as

$$\mathcal{F} = \frac{r^2(\tau_y + K\dot{\gamma}^n)}{\mathcal{A}} - 1 = 0 \quad \text{for} \quad |\dot{\gamma}| > 0. \tag{2}$$

We thus have to seek for the roots of $\mathcal{F}$ to evaluate the unknown parameters τ_y, K, n and M. As the rheological parameters are only a function of the solution used, the following procedure is therefore applied for Carbopol A and Carbopol B independently. For a given solution, N_α experiments were performed, only the amplitude Ω_0 being varied. In Eq. (2), the numerator $\mathcal{A}$ depends only on Ω_0 through the modification of the imposed torque M, and will be noted in the following $\mathcal{A}_\alpha$, i.e. as a function of the experiment label α. According to this, τ_y, K and n then minimize

$$\mathcal{S} = \frac{1}{N_\alpha} \sum_\alpha \sum_i \left(\mathcal{F}_{\alpha,i}\right)^2, \tag{3}$$

where label i stands for the spatial discretization and the discrete functional $\mathcal{F}_{\alpha,i}$ reads

$$\mathcal{F}_{\alpha,i} = \frac{r_i^2\left(\tau_y + K\left(\dot{\gamma}_{\alpha,i}\right)^n\right)}{A_\alpha} - 1, \quad A_\alpha = \frac{1}{N_{\alpha,i}} \sum_i r_i^2\left(\tau_y + K\left(\dot{\gamma}_{\alpha,i}\right)^n\right), \tag{4}$$

with $N_{\alpha,i}$ the number of spatial mesh in the shear zone, i.e. such as $|\dot{\gamma}_{\alpha,i}| > 0$. The best estimation of τ_y, K and n can then be obtained using a Newton–Raphson method.

Values of τ_y, K, n obtained with this method for Carbopol *A* and Carbopol *B* are given in Table 1 (bottom row). In Fig. 1, the τ to $\dot{\gamma}$ laws derived from this method (solid lines) are compared with the rheometric measurements, presented in Section 2.1. As can be observed from these comparisons, a very good agreement is obtained between the different methods.

4. Oscillatory flows: The unsteady shear configuration

4.1. Some key features of the flow dynamics

In the range of parameters used in this study, oscillatory experiments were shown to be $T(=2\pi/\omega)$-periodic in the entire cell gap after the first forcing period. Azimuthal Velocity profiles $v(r,t)$ extracted from the PIV measurement are therefore phase averaged from the second period to the end of the experiments, the number of period depending on the forcing parameters Ω_0 and ω. In the following, only phase averaged variables are presented and discussed, the experimental time being therefore reduce to a single forcing period with $t \in [0\ T]$. As no confusion can occur from hereon, variable names are unchanged.

Typical experimental results obtained in the case of an applied oscillatory forcing, i.e. $\Omega_i = \Omega_0 \sin(\omega t)$, are shown in Fig. 5 for $\Omega_0 = 30$ rpm and $T = 2\pi/\omega = 10$ s. Velocity profiles are shown in Fig. 5(a) and (b) for Carbopol *A* and Carbopol *B* respectively. Here, only the first quarter of the forcing period, $t \in [0\ T/4]$, is presented for sake of clarity. It corresponds to the time interval in which the applied angular velocity increases from 0 to its maximum amplitude Ω_0. Note that, a surprisingly large velocity invading the entire gap of the Couette cell is observed on a quite short time scale for the parameters of these experiments. This specific velocity trend will be discussed in the next sections. The associated deformations $u = \int_0^t v dt$ of the gel are shown in Fig. 5(c) and (d) for Carbopol *A* and Carbopol *B* respectively. Note that the deformation applied at the inner cylinder radius with the angular law used here, is $u(R_i,t) = \frac{\Omega_0}{\omega} R_i(1 - cos(\omega t))$.

Two specific behaviors are highlighted in Fig. 5. A non-zero velocity amplitude is first observed on the entire Couette gap at a relatively short time scale, which is followed by the evolution of a shear zone localized close to the inner cylinder while the outer region has zero velocity. This second phase is comparable to the steady shear configuration, for which the shear band width was shown to depend on the rheological properties of the gel (see Fig. 4) as again observed here (Fig. 5(a) for Carbopol *A* compared with Fig. 5(b) for Carbopol *B* for instance). It can also be noted that the shear flow during this phase shows common trends with the viscoplastic Stokes layer studied by [21]. In particular, a time dependent shear band, which corresponds to a fluid behavior is observed in the two cases close to the oscillating boundary. However, the plug flow in the solid region observed in their case is here replaced by an elastic solid subjected to unsteady deformations. Such elastic deformations correspond to non-zero velocities observed on the entire cell gap at early stages of the forcing period (see Fig. 5(a) and (b)). This elastic contribution is highlighted in term of elastic deformation in Fig. 5(c) and (d). In these figures, the maximum deformation is shown to be of the order of few centimeters in the zone which remains frozen when the inner region becomes clearly fluid ($r > 9.5$ cm for Carbopol *A* and $r > 8.5$ cm for Carbopol *B*). Note that this deformation does not relax in the frozen zone. The entire period $[0\ T]$ has to be considered to help understanding the complete cycle of the elastic deformation over the forcing period (see Fig. 6 for the same case as Fig. 5(a) and (c)). One can then note that the frozen state corresponds to a steady state of the elastic deformation over the first half period, $t \in [0\ T/2]$. When the inner cylinder velocity $v(R_i,t)$ becomes negative, i.e. for $t \in [T/2\ T]$, the deformation goes back to zero on the same time scale as the initial elastic deformation. Therefore, for this range of parameters, a steady state regime is reached in the solid zone with a non-zero deformation, which only goes back to its initial state when the opposed forcing is imposed to the system.

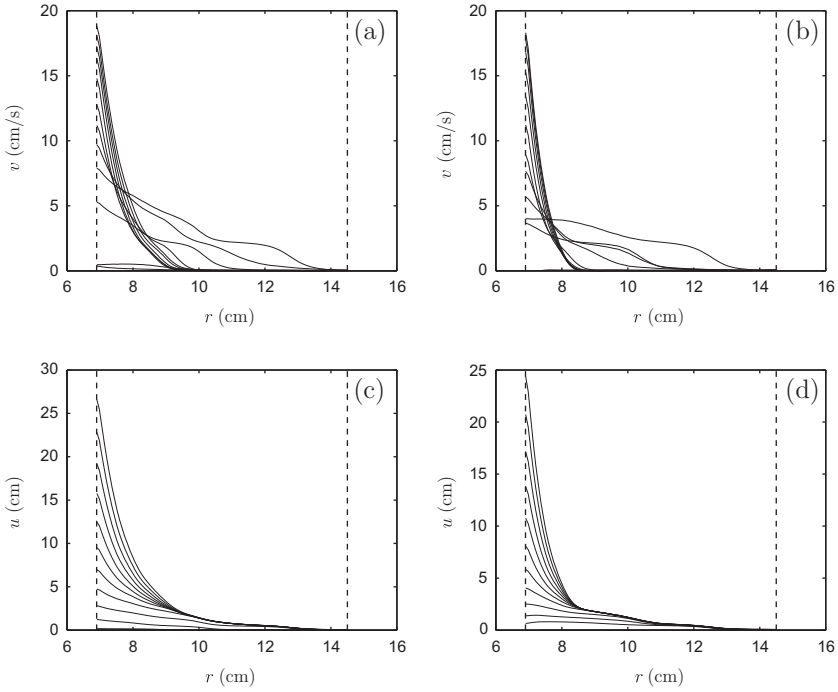


Fig. 5. (a) Velocity profiles $v(r,t)$ with $t \in [0\ T/4]$ for Carbopol *A*, $\Omega_0 = 30$ rpm and $T = 2\pi/\omega = 10$ s. (b) Same as (b) for Carbopol *B*. (c) Deformation profiles $u(r,t)$ with $t \in [0\ T/4]$ for Carbopol *A*, $\Omega_0 = 30$ rpm and $T = 2\pi/\omega = 10$ s. (d) Same as (d) for Carbopol *B*.

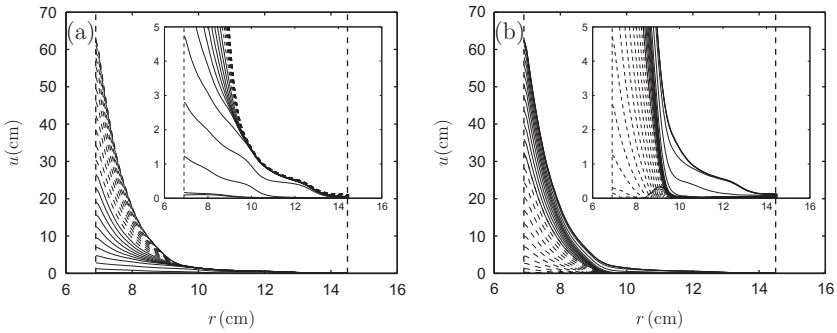


Fig. 6. Deformation profiles $u(r,t)$ for Carbopol *A*. (a) $t \in [0\ T/2]$ (solid lines: $t \in [0\ T/4]$; dotted lines: $t \in [T/4\ T/2]$), and (b) $t \in [T/2\ T]$ (solid lines: $t \in [T/2\ 3T/4]$; dotted lines: $t \in [3T/4\ T]$). (Insets: zooms on the elastic zone).

Quasi-steady states solutions will be derived in Section 4.2 for comparisons with these observations. Note that the initial state of the gel is nearly recovered at the end of the forcing period for this set of parameters.

To understand the dynamics described so far, the contribution of both viscoplastic and elastic effects have to be accounted for. In particular, how does elasticity affect the whole dynamics of the system and possibly the fluid/solid transition in such a configuration? First, let us discuss the pertinent dimensionless numbers in this configuration. The set of dimensionless numbers is obtained using $1/\omega$ as a typical time scale, R_i the length scale and ΩR_i the velocity scale and the Herschel–Bulkley model for the viscous contribution. For the latter model, the extra dimensionless number n is introduced. Using the Herschel–Bulkley model for the viscoplastic contribution, we can write a relaxation time as $\lambda = K\Omega_0^{n-1}/G$ [4] and an equivalent viscosity $\nu_e = K\Omega_0^{n-1}$. Moreover, the shear stress is non-dimensionalised using its typical viscous contribution $\Omega_0^n K$. It therefore leads to the following definitions of the dimensionless numbers

$$\mathrm{Bi} = \frac{\tau_y}{\Omega_0^n K}, \quad \mathrm{De} = \frac{K}{G}\omega\Omega_0^{n-1}, \quad \mathrm{Re} = \frac{\rho\omega\Omega_0^{1-n}R^2}{K}. \tag{5}$$

The Bingham number, Bi, compares the plastic yield stress to the viscous stress. The Deborah number De is the dimensionless relaxation time of elastic energy stored in the gel. At small De, the flow remains viscoplastic while it becomes mostly elastic at larger De. Note that De is here similar to the Weissenberg number We [24,5]. Finally, the Reynolds number Re is the ratio between the viscous time scale and the inertial time scale, with here the viscous time scale being built on an equivalent viscosity.

In the following, all variables are non-dimensionalised accordingly. Note that for simplicity, names of variables in their dimensionless form are kept the same. In dimensionless variables, the geometry of the system is then defined in the interval $r \in [1\ R_o]$ and the forcing period is such as $t \in [0\ 2\pi]$.

4.2. Quasi-steady state models

A first attempt to describe the fluid flow is to assume that its evolution remains quasi-steady. In this case, the flow is a succession of steady solutions whose boundary conditions are related to the velocity applied to the inner cylinder $v(R_i,t)$ at a given time $t \in [0\ T]$. In the following, a purely viscoplastic model and a purely elastic model are presented to highlight both phenomenon in the material. In the first case, a purely visco-plastic fluid which does not account for elastic deformations in its solid region, is assumed. On the other hand, in the second model, one considers a purely elastic deformation of the gel which does not reach a plastic threshold on the entire cell gap.

If the oscillatory flow is considered as quasi-steady and the fluid rheology is modeled by a Herschel–Bulkley model, i.e. a purely viscoplastic fluid, the governing equations reduce to

$$\tau = \mathrm{Bi}_{qs}\left(\frac{r_c}{r}\right)^2, \quad \tau = \mathrm{Bi}_{qs} + \dot{\gamma}^n, \tag{6}$$

with $\dot{\gamma} = r\frac{\partial}{\partial r}(v/r)$, and $r_c = r(\tau = \mathrm{Bi})$ the critical radius which characterizes the fluid–solid transition. In the present quasi-steady model, Bi_{qs} is defined using the instantaneous angular velocity Ω_i instead of Ω_0 as in Bi. It therefore means that the lost time dependance of the model is then incorporated in Bi_{qs} through the instantaneous angular velocity at $r = 1$. In particular $\mathrm{Bi}_{qs} = \mathrm{Bi}$ at $t = T/4$. A pseudo-theoretical solution can be derived for the fluid region, i.e. $r < r_c$ [5]

$$v(r) = r\int_r^{r_c} \frac{\mathrm{Bi}_{qs}^{1/n}}{x}\left[\left(\frac{r_c}{x}\right)^2 - 1\right]^{1/n}, \tag{7}$$

the solution for $r > r_c$, i.e. in the solid region, being $v(r) = 0$. The critical radius is thus defined as

$$\int_1^{r_c} \frac{\mathrm{Bi}_{qs}^{1/n}}{x}\left[\left(\frac{r_c}{x}\right)^2 - 1\right]^{1/n} - 1 = 0. \tag{8}$$

Solutions of (7) and (8) are found here using a Newton–Raphson algorithm to obtain r_c as a function of (Bi_{qs}, n) and a recursive adaptive Lobatto quadrature (Matlab©) for the integral terms. Such solutions are compared with the experimental velocity profiles in Fig. 7 for the set of parameters (a) $(\mathrm{Bi},\mathrm{Re},\mathrm{De},n) = (1.5, 1.7, 0.014, 0.44)$, (b) $(\mathrm{Bi},\mathrm{Re},\mathrm{De},n) = (1.5, 8.5, 0.07, 0.44)$, (c) $(\mathrm{Bi},\mathrm{Re},\mathrm{De},n) = (2.35, 0.34, 0.014, 0.4)$ and (d) $(\mathrm{Bi},\mathrm{Re},\mathrm{De},n) = (2.35, 0.69, 0.028, 0.4)$. Here experimental results are presented for $t \in [0\ T/4]$ (gray lines in Fig. 7). In all cases, steady state theoretical solutions (7) are given at $t = T/8$ and $t = T/4$, using corresponding Bi_{qs} (dotted black lines). These two lines provide an interval of expected existence of the viscous region, at least when a quasi steady state is expected, i.e. for sufficiently small Re. In most cases, the theoretical solution matches the experimental profiles around $t = T/4$, meaning that a quasi-steady state is reached (see Fig. 7(a), (c), and (d)). In these cases, Bi is found to affect the value of r_c as expected. However, one can see that transient profiles but also the case $(\mathrm{Bi},\mathrm{Re},\mathrm{De},n) = (1.5, 8.5, 0.07, 0.44)$ (Fig. 7(b)) do not follow this profile law. In particular, velocity profiles larger than the solution at $t = T/4$, which should maximize the velocity for a purely viscoplastic fluid in a quasi-steady state regime, are highlighted. In such cases, unsteadiness and elastic contribution cannot be disregarded and are considered in the following. We thus anticipate an influence of Re and De.

In a similar way, if one assumes a purely elastic deformation associated with the oscillatory forcing, a quasi steady state solution can then be sought in term of the deformation $u(r)$. Such solution then reads

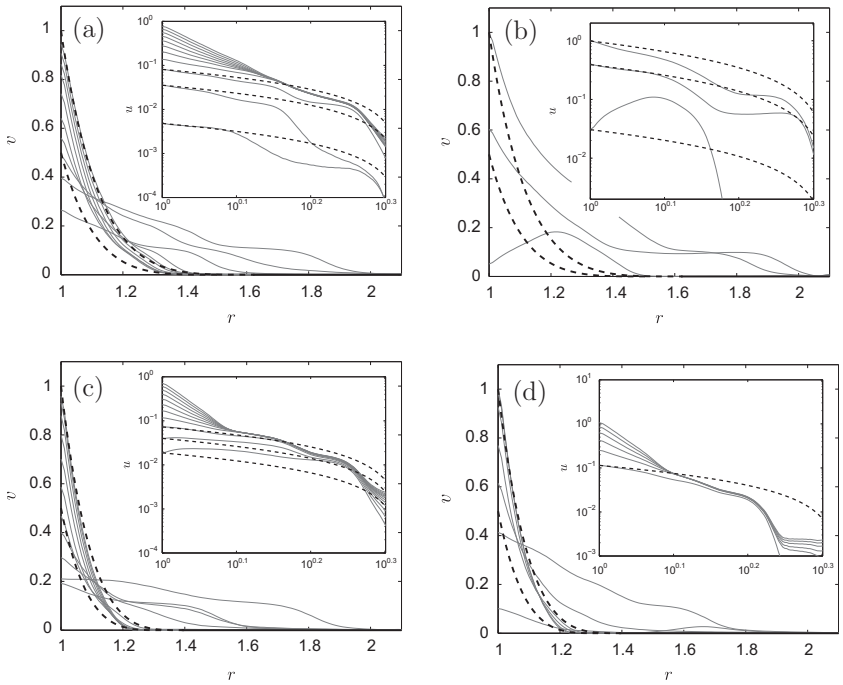


Fig. 7. Radial velocity profiles $v(r,t)$ on the first quarter of the oscillating period for (a) $(\mathrm{Bi},\mathrm{Re},\mathrm{De},n) = (1.5, 1.7, 0.014, 0.44)$, (b) $(\mathrm{Bi},\mathrm{Re},\mathrm{De},n) = (1.5, 8.5, 0.07, 0.44)$, (c) $(\mathrm{Bi},\mathrm{Re},\mathrm{De},n) = (2.35, 0.34, 0.014, 0.4)$ and (d) $(\mathrm{Bi},\mathrm{Re},\mathrm{De},n) = (2.35, 0.69, 0.028, 0.4)$. Gray lines correspond to the experimental results while dotted black lines are theoretical solutions obtained from the steady-state approximation (7). (Inset: corresponding deformation u).

$$u(r) = \frac{u_i}{R_o^2 - 1}\left(\frac{R_o^2}{r} - r\right), \tag{9}$$

with u_i being the applied deformation at $r = 1$. Here, one assumed no deformation of the material at $r = R_o$. Such solutions are compared with the experimental deformation u in Fig. 7 (inlet) for the same set of parameters considered previously. Once again, only $t \in [0\ T/4]$ is shown here. Even if the quantitative agreement is not clear on the whole r range, solution (9) seems to be pertinent close to the inner cylinder at the initial stage of the forcing period, at least for cases (a) and (c) in Fig. 7. Once again, unsteadiness is needed to understand the whole coupled dynamics of the system for the set of dimensionless parameters considered here. In the next section, we propose an unsteady model, based on [6,7], which accounts for these different observations.

4.3. Elasto-viscoplastic model

Following [6,7,5], an elasto-viscoplastic model including both the viscoplastic and the elastic contributions encountered in the Carbopol gel, is developed to describe the experimental observation of the unsteady shear configuration. As done in [4,7], the extension of the Saramito's model of a Bingham viscoplastic contribution [6] to the Herschel–Bulkley viscoplastic model is used here, while the loss modulus G'' is disregarded as it was found to be much smaller than the elastic contribution G (see Table 1). Moreover, for simplicity, the tensorial derivative of the stress $D\tau/Dt$ introduced in these models, such as the upper-convective derivative of the Oldroyd model for instance, is simplified to a scalar version as done in [4]. The only non-zero stress component is therefore the shear stress, whose temporal evolution does not account for complex non-linear contributions. The non-linear term would introduce a coupling between shear flow and extensional flow. Such terms can then affect the steady state solution as highlighted by [5]. However, these non-linearities were shown to be a second order contribution to the steady state solution, and are therefore anticipated to be much smaller than the unsteady contribution in the present configuration. Using the dimensionless numbers defined previously, the set of simplified equations for an axisymmetric rotating flow of an elasto-viscoplastic gel can then be written as

$$\mathrm{Re}\frac{\partial v}{\partial t} = \frac{1}{r^2}\frac{\partial}{\partial r}(r^2\tau), \tag{10a}$$

$$\mathrm{De}\frac{\partial \tau}{\partial t} = \dot{\gamma} - \max\left[0; |\tau| - \mathrm{Bi}\right]^{1/n}\frac{\tau}{|\tau|}. \tag{10b}$$

Note that the first contribution of the right hand side of Eq. (10b) corresponds to the elastic part of the model, which is equivalent to an elastic Hooke law in the present case, while the second term is the viscoplastic part, including the yield component. The aim of the above mentioned simplifications is to reduce the problem to a set of only two equations (instead of four with an upper-convective model for instance). Eqs. (10a) and (10b) are then straightforward to solve numerically without losing the physical process of the unsteady dynamics as shown in the following. Here, a second order Adams–Bashforth explicit scheme in time and a second order finite difference scheme for spatial derivatives are used. In order to avoid amplification of numerical noise, a small dissipation term is added according to the retardation parameter defined in Saramito's model [7] (their Eq. (7)). This term is somehow related to the loss modulus, but is not explicitly derived here and is only used as a numerical filter. It has been verified that this extra term does not modify the results presented in the following.

A comparison between the experimental results and the model is shown in Fig. 8 for different sets of non dimensional parameters, $(\mathrm{Bi},\mathrm{De},\mathrm{Re}) = (2, 0.01, 0.3)$ (Fig. 8(a)), $(\mathrm{Bi},\mathrm{De},\mathrm{Re}) = (4, 0.04, 0.4)$ (Fig. 8(b)) and $(\mathrm{Bi},\mathrm{De},\mathrm{Re}) = (2, 0.1, 4.6)$ (Fig. 8(c)), and $n \approx 0.4$. Fig. 8(a.1, b.1, c.1) and (a.2, b.2, c.2) show the spatio-temporal diagrams of the non-dimensional velocity $v(r,t)$ over the period $t \in [0\ T]$, obtained from PIV measurements and the elasto-viscoplastic model (10a) and (10b) respectively. Moreover, the fluid/solid transition, i.e. $\tau(r,t) = \tau_y$ is also extracted from the model

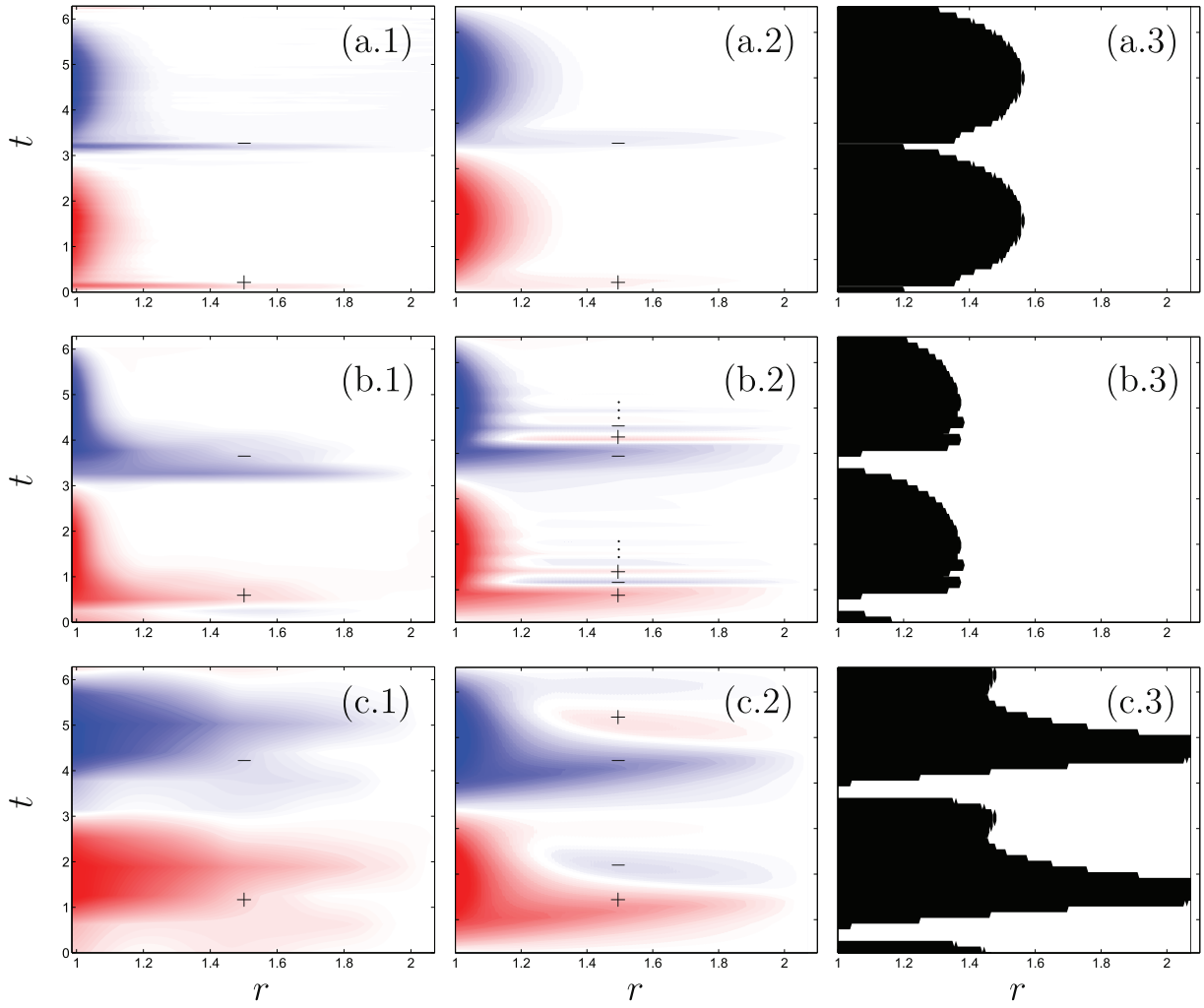


Fig. 8. Spatio-temporal diagram $v(r,t)$ extracted from experimental data (a.1–c.1) and numerical model (a.2–c.2) (online color: blue (resp. red) corresponds to negative (resp. positive) velocity v; -/+ symbols also show the sign of v for gray scale printing). (a.3–c.3) show the fluid/solid transition obtained from the numerical model (fluid: black, solid:white). Non-dimensional parameters are $n \approx 0.4$ and (a) $(\mathrm{Bi},\mathrm{De},\mathrm{Re}) = (2, 0.01, 0.3)$, (b) $(\mathrm{Bi},\mathrm{De},\mathrm{Re}) = (4, 0.04, 0.4)$ and (c) $(\mathrm{Bi},\mathrm{De},\mathrm{Re}) = (2, 0.1, 4.6)$. (For interpretation to colours in this figure, the reader is referred to the web version of this paper.)

(see Fig. 8(a.3,b.3,c.3) in which black and white areas correspond to a fluid phase and a solid phase respectively). One can first note that the dynamics of such an elasto-viscoplastic fluid is nicely reproduced by the numerical model in the range of parameters considered here, despite the assumptions mentioned previously. Note that, most of the quantitative discrepancy can be associated with the acquisition rate used for in the experiments, with which elastic time is hardly reached.

While the dynamics resembles the case of a purely viscoplastic fluid in Fig. 8(a), the dynamics is shown to be more complex otherwise (Fig. 8(b) and (c)). The latter observation is confirmed by the time evolution of the shear stress τ, as shown in Fig. 9. In particular, Fig. 9(a) shows that the shear stress evolution is nearly singular at each half period (zero velocity forcing), with a jump from $-\mathrm{Bi}$ to Bi as expected for a purely visco-plastic fluid. For the other cases (Fig. 9(b) and (c)), the shear stress evolution is quite different. In particular, we can note that the previously mentioned stress jump is smoothed over a significant time interval. Moreover, a time lag of the zero stress value at the inner cylinder appears in these cases.

In order to highlight the physical contributions in these complex dynamics, let us discuss the influence of the dimensionless parameters. Beyond their individual definition given previously, it is shown from Eqs. (10a) and (10b) that the dynamics of the oscillatory flows is controlled by several balances depending on the relative contribution of these numbers. In particular, one can highlight an elastic–plastic balance $\mathrm{BiDe} = \frac{\gamma_c}{\Omega/\omega}$ with $\gamma_c = \tau_y/G$ an estimation of the critical shear as defined in Section 2, a plastic-inertial balance $\mathrm{Bi}/\mathrm{Re} = \tau_y/(\rho\Omega\omega R^2)$ and an elastic-inertial balance $\mathrm{ReDe} = \rho\omega^2 R^2/G$. The latter contribution will be discussed in more detail in Section 4.4. For now, it could be just noted that when ReDe increases (from (a) to (c) in Figs. 8 and 9), a complex dynamics invades the entire cell on nearly the whole time period while the stress component highlights the specific evolution described previously. These observations are attributed to an elastic contribution whose propagation information along the radial direction seems to decrease with ReDe. The two other contributions BiDe and Bi/Re relate the relative contribution of the plastic yield with elasticity and inertia. In particular, $\mathrm{BiDe} \gg 1$ indicate a dominant elastic contribution in the entire cell gap, since γ_c then remains larger than Ω/ω, i.e. the maximum elastic deformation of the gel prior yielding is large compared with the maximum deformation imposed by the inner forcing. Otherwise, plastic yielding can occur in the system, leading to a localized shear band, which first appears in the vicinity of the inner boundary $r = 1$ where the deformation is maximum. In particular, increasing BiDe indicates a longer time scale of elastic deformation close to the inner cylinder prior yield-

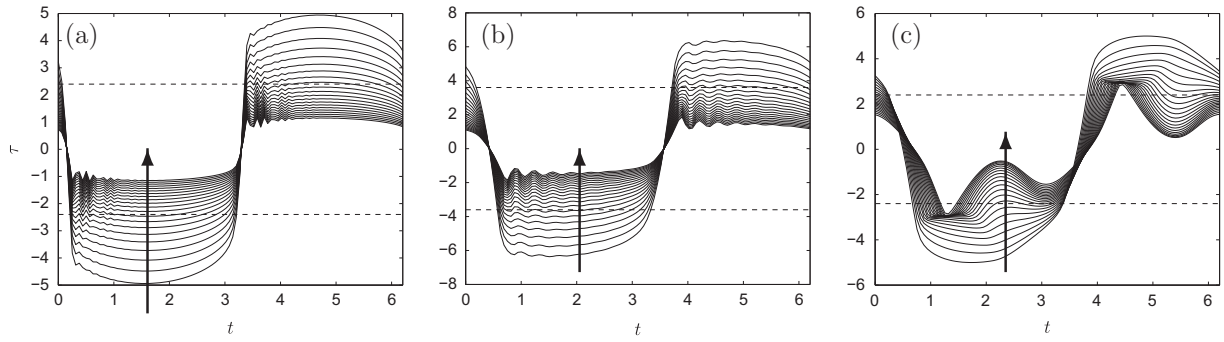


Fig. 9. τ as a function of time t over a period of forcing at different radial position r, obtained from the numerical modeling. Arrows indicate the direction of increasing r from the inner cylinder to the outer cylinder. Parameters set are the same as the ones presented in Fig. 8. Dotted line corresponds to the plastic threshold $\tau_y = \pm$Bi.

ing, relative to the time scale of the forcing period. This trend is observed in Fig. 8 (third column) where BiDe increases from (a) to (c). On the other hand, Bi/Re gives an indication on the width of the fluid shear region in the vicinity of $r = 1$. In particular, $\mathrm{Bi}/\mathrm{Re} \gg 1$ corresponds to a narrow shear zone due to a large contribution of the plastic threshold, while this zone is expected to invade the cell for $\mathrm{Bi}/\mathrm{Re} \ll 1$. Once again, this is in accordance with experimental and modeling results shown in Fig. 8, in which the extension of the fluid shear region increases for decreasing Bi/Re ((b)–(a)–(c) in Fig. 8).

A quantitative information which can be extracted from these data is the normalized kinetic energy E_k, which is defined as

$$E_k = \int_0^{2\pi} \int_1^{R_o} u^2(r,t) r dr dt. \tag{11}$$

According to the previous discussion, this quantity is considered in the $(\mathrm{Bi}/\mathrm{Re}, \mathrm{BiDe})$ parameter space (see Fig. 10). The amplitude of E_k is here represented by gray levels for both symbols (experiments) and solid lines (numerical modeling), with in particular E_k which increases from light gray to black (see legend in Fig. 10). Note that a given value of BiDe could correspond to different couples $(\mathrm{Bi}, \mathrm{De})$, giving rise to different value of E_k. Values of $(\mathrm{Bi}, \mathrm{De})$ used in the numerical modeling for each constant BiDe have therefore been chosen to be consistent with the experimental parameters. The obtained range of variation between experimental parameters and numerical modeling have been shown to be relatively small. Fig. 10 therefore allows to give a first general picture of the kinetic energy in the system over a period of oscillation. One can note that the predicted kinetic Energy E_k in the system, using the numerical model, is in quantitative agreement with experimental results in the range of the considered parameters despite the simplicity of the model. Moreover, this figure shows an overall increase of the kinetic energy with increasing BiDe and a maximum for Bi/Re around unity. This trend is associated with an increasing contribution of the elastic energy when BiDe increases for not too small Bi/Re. When Bi/Re becomes large, flow inertia decreases and the resulting kinetic energy decreases with it.

4.4. Elastic waves

To finish with, the dynamics of the elastic front on each half-period, highlighted in Fig. 8, is discussed in the following in term of elastic wave. For this purpose, a purely elastic regime, i.e. below the plastic yield stress τ_y, is considered here. In this case, Eqs. (10a) and (10b) can be reduced to

$$\mathrm{ReDe}\frac{\partial^2 v}{\partial t^2} = \frac{1}{r^2}\frac{\partial}{\partial r}(r^2\dot{\gamma}), \tag{12}$$

which in term of the vertical vorticity $\zeta = \frac{1}{r}\frac{\partial}{\partial r}(rv)$ can be simplified to the wave equation

$$\mathrm{ReDe}\frac{\partial^2 \zeta}{\partial t^2} = \nabla^2\zeta, \tag{13}$$

with $\nabla^2 = \frac{\partial^2}{\partial r^2} + \frac{1}{r}\frac{\partial}{\partial r}$, the laplacian operator in cylindrical coordinates. Eq. (13) describes the evolution of an elastic shear wave. Seeking for waves solutions of the form $f(r)\exp(-ist)$, with s the wave frequency, Eq. (13) reduces to a Helmholtz equation, whose solutions can be written as

$$\zeta(r,t) = (AJ_0(kr) + BY_0(kr))\exp(-ist) + c \cdot c, \tag{14}$$

where A and B are constants which can be found from boundary conditions, k is a spatial wave number such as $c_\phi = s/k = (\mathrm{ReDe})^{-1/2}$. In order to highlight the elastic wave structure which could be encountered in the unsteady Couette configuration, we will focus in the following on the asymptotic expansions for the wave number k of the general solution (14). The aim of the present section is therefore not to give the complete solution of (14) subjected to boundary conditions. First, a large k solution can be found using asymptotic expansion of the Bessel functions [25].

$$\zeta(r,t) \approx \left(A\sqrt{\frac{2}{\pi kr}}\cos(kr - \pi/4) + B\sqrt{\frac{2}{\pi kr}}\sin(kr - \pi/4)\right)\exp(-ist) + c \cdot c, \tag{15}$$

which is similar to 1D planar wave solution but with a $r^{-1/2}$ amplitude decrease with the spatial coordinate. Note that the solution for the velocity v could be found in terms of Bessel functions of the form $J_1 kr$ and $Y_1 kr$ which also shows a $r^{-1/2}$ trend for large argument expansion. In the other limit, i.e. when k goes to zero, one obtains [25]

$$\zeta(r,t) \approx \left(A + B\frac{2}{\pi}\left(\ln\frac{kr}{2} + \tilde{\gamma}\right)\right)\exp(-ist) + c \cdot c, \tag{16}$$

with $\tilde{\gamma} \approx 0.5772$ the Euler-Mascheroni constant. Similar expansions can also be found for the velocity component v, leading to a r^{-1} trend for its wave amplitude along the radial direction. Note that the latter expansion is not expected to be encountered in a confined domain such as the present geometry of the system.

Unfortunately, even if a r dependance is clearly observed with the experimental data, in particular an amplitude decreasing from the inner cylinder to the outer one, it is difficult to confirm, in the state, the power law dependance on r obtained with the asymptotic expansion. Dedicated experiments would probably be necessary to validate the model, and are postponed to a future work. Nevertheless, the velocity of the propagating front c_ϕ can be extracted from the experimental data. In particular, c_ϕ is plotted as a function of ReDe in Fig. 11. Even if data are slightly dispersed, mainly due to the recording rate of the camera, the obtained front propagation clearly highlight a $(\mathrm{ReDe})^{-1/2}$ trend (dotted line in

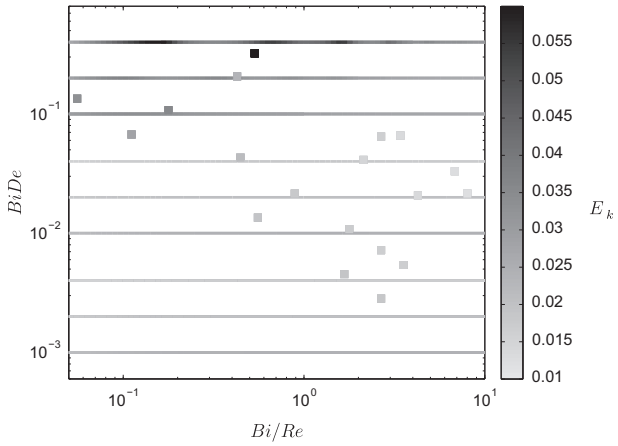


Fig. 10. Kinetic energy E_k in the (Bi/Re, BiDe) plane. Square symbols correspond to the set of experiments while solid lines are obtained from the numerical model. Amplitude of E_k corresponds to the gray level of the different symbols. Constant BiDe lines obtained from numeric modeling correspond to the parameters couples $(\mathrm{Bi}, \mathrm{De}) = [(1, 10^{-3}), (1, 10^{-2}), (1, 10^{-1}), (2, 10^{-3}), (2, 10^{-2}), (2, 10^{-1}), (4, 10^{-3}), (4, 10^{-2}), (4, 10^{-1})]$ from bottom to top.

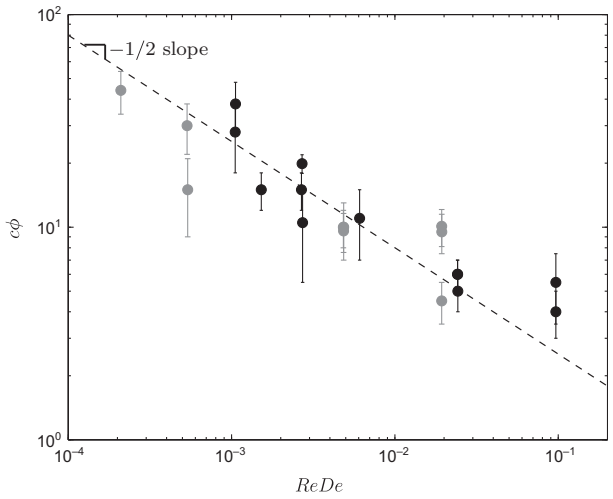


Fig. 11. Velocity of the propagating elastic front c_ϕ as a function of ReDe for Carbopol *A* (black dots) and Carbopol *B* (gray dots). The dotted line corresponds to a $(ReDe)^{-1/2}$ law.

Fig. 11). It therefore confirms the existence of an elastic wave, which propagates from the inner cylinder towards the outer one, showing a $(\mathrm{ReDe})^{-1/2}$ trend in accordance with the relation of dispersion of elastic waves.

5. Conclusion

A PIV method has been developed to measure the velocity field of a Carbopol gel in a large cylindrical Couette cell. Both steady and unsteady sheared flows have been studied by applying a constant angular velocity and an oscillatory angular velocity to the inner cylinder. In the steady state regime, an inverse method has been proposed to extract the rheological properties of the gel from the only velocity profiles of the gel flow. Results obtained with this method have shown to be in good agreement with the rheological parameters obtained with a Thermo-Scientific HAAKE Mars III rheometer. In the unsteady regime, a complex dynamics, which involved elastic and viscous contribution of the gel has been highlighted. Such dynamics has been discussed in terms of the non-dimensional parameters, Bi, Re, De, and to a lesser extent n, by developing different models. In particular, quasi-steady states models, $\mathrm{Re} \ll 1$, can describe both the viscous shear zone in the vicinity of the inner cylinder and the elastic deformation at early stages of the forcing period, when these two contributions are not strongly coupled. Moreover, an elasto-viscoplastic model, based on [6,7], has been developed to account for unsteadiness of the flow. Now, elastic and viscoplastic contributions can coexist in the cell gap. Such model is shown to quantitatively reproduce the dynamics observed in the experiments even for strongly unsteady cases. Moreover, the numerical results emphasize the contribution of the elastic component on the dynamics compared with a localized shear zone which would be obtained for a purely viscoplastic model. Finally, the propagation of the elastic deformation from the inner cylinder to the outer one has been described by an elastic front whose propagation is related to the phase velocity of elastic waves.

Acknowledgements

Authors would like to thank N.J. Balmforth and an anonymous reviewer for very helpful comments on the paper. Authors are grateful for helpful discussions on viscoplastic fluid dynamics with Dominique Anne-Archard, and also for providing the Carbopol. LL and AF thank Sébastien Cazin for support on PIV measurements.

References

[1] N.J. Balmforth, I.A. Frigaard, G. Ovarlez, Viscoplastic fluids in nature and industry, Ann. Rev. Fluid Mech. 46 (1) (2014).
[2] J. Piau, Carbopol gels: elastoviscoplastic and slippery glasses made of individual swollen sponges: meso- and macroscopic properties, constitutive equations and scaling laws, J. Nonnewton. Fluid Mech. 144 (1) (2007) 1–29.
[3] H. Tabuteau, D. Sikorski, J.R. de Bruyn, Shear waves and shocks in soft solids, Phys. Rev. E 75 (2007) 012201.
[4] L.-H. Luu, Y. Forterre, Drop impact of yield-stress fluids, J. Fluid Mech. 632 (1) (2009) 301–327.
[5] I. Cheddadi, P. Saramito, F. Graner, Steady Couette flows of elastoviscoplastic fluids are nonunique, J. Rheol. 56 (2012) 213.
[6] P. Saramito, A new constitutive equation for elastoviscoplastic fluid flows, J. Nonnewton. Fluid Mech. 145 (1) (2007) 1–14.
[7] P. Saramito, A new elastoviscoplastic model based on the Herschel–Bulkley viscoplastic model, J. Nonnewton. Fluid Mech. 158 (1–3) (2009) 154–161.
[8] Y.S. Park, P.L.-F. Liu, Oscillatory pipe flows of a yield-stress fluid, J. Fluid Mech. 658 (2010) 211–228.
[9] J.J. Stickel, J.S. Knutsen, M.W. Liberatore, Response of elastoviscoplastic materials to large amplitude oscillatory shear flow in the parallel-plate and cylindrical-Couette geometries, J. Rheol. (1978-present) 57 (6) (2013) 1569–1596.
[10] G. Ovarlez, S. Rodts, X. Chateau, P. Coussot, Phenomenology and physical origin of shear localization and shear banding in complex fluids, Rheol. Acta 48 (8) (2009) 831–844.

[11] T. Divoux, D. Tamarii, C. Barentin, S. Manneville, Transient shear banding in a simple yield stress fluid, Phys. Rev. Lett. 104 (20) (2010) 208301.
[12] G. Ovarlez, S. Cohen-Addad, K. Krishan, J. Goyon, P. Coussot, On the existence of a simple yield stress fluid behavior, J. Nonnewton. Fluid Mech. 193 (2013) 68–79.
[13] G. Debregeas, H. Tabuteau, J.-M. Di Meglio, Deformation and flow of a two-dimensional foam under continuous shear, Phys. Rev. Lett. 87 (17) (2001) 178305.
[14] P. Coussot, J. Raynaud, F. Bertrand, P. Moucheront, J. Guilbaud, H. Huynh, S. Jarny, D. Lesueur, Coexistence of liquid and solid phases in flowing soft-glassy materials, Phys. Rev. Lett. 88 (21) (2002) 218301.
[15] C. Gilbreth, S. Sullivan, M. Dennin, Flow transitions in two-dimensional foams, Phys. Rev. E 74 (5) (2006) 051406.
[16] P. Schall, M. van Hecke, Shear bands in matter with granularity, Annu. Rev. Fluid Mech. 42 (1) (2009) 67.
[17] A. Magnin, J. Piau, Cone-and-plate rheometry of yield stress fluids. Study of an aqueous gel, J. Nonnewton. Fluid Mech. 36 (1990) 85–108.
[18] S. Curran, R. Hayes, A. Afacan, M. Williams, P. Tanguy, Properties of Carbopol solutions as models for yield-stress fluids, J. Food Sci. 67 (1) (2002) 176–180.
[19] A.M. Putz, T.I. Burghelea, The solid–fluid transition in a yield stress shear thinning physical gel, Rheol. Acta 48 (6) (2009) 673–689.
[20] A. Magnin, J. Piau, Shear rheometry of fluids with a yield stress, J. Nonnewton. Fluid Mech. 23 (1987) 91–106.
[21] N.J. Balmforth, Y. Forterre, O. Pouliquen, The viscoplastic Stokes layer, J. Nonnewton. Fluid Mech. 158 (1) (2009) 46–53.
[22] A. Fincham, G. Delerce, Advanced optimization of correlation imaging velocimetry algorithms, Exp. Fluids 29 (1) (2000) S013–S022.
[23] P. Coussot, L. Tocquer, C. Lanos, G. Ovarlez, Macroscopic vs. local rheology of yield stress fluids, J. Nonnewton. Fluid Mech. 158 (1–3) (2009) 85–90.
[24] I. Cheddadi, P. Saramito, C. Raufaste, P. Marmottant, F. Graner, Numerical modelling of foam Couette flows, Eur. Phys. J. E 27 (2) (2008) 123–133.
[25] M. Abramowitz, I.A. Stegun, Handbook of Mathematical Functions: With Formulas, Graphs, and Mathematical Tables, vol. 55, Courier Dover Publications, 1972.